CrossMark
click for updates

Synthesis of efficient near-infrared-emitting CuInS2/ZnS quantum dots by inhibiting cation-exchange for bio application†

Yi su Kim,‡ Yonghee Lee,‡ Youngsun Kim,§ Donghyuk Kim, Hyung Seok Choi, Jae Chul Park, Yoon Sung Nam* and Duk Young Jeon*

Near-infrared (NIR)-emitting CuInS2(CIS)/ZnS quantum dots (QDs) were synthesized using an off-stoichiometry effect, and the tuned emission wavelength was 850 nm, which is suitable for deep tissue imaging. Due to the unintentional occurrence of cation exchange, however, the emission wavelength of the synthesized CIS core was blue-shifted after ZnS shell coating. In order to inhibit this blue-shift, controlling the synthesis temperature during ZnS shell coating was required, and the selected synthesis temperatures were 180 °C, 210 °C, 230 °C, and 250 °C. The effect of temperature on the emission properties of CIS/ZnS QDs could be related to substitutional diffusion of Zn^{2+} ions, as expressed by Fick's law. The least blue-shifted emission wavelength was 810 nm and the amount of blue-shift was about 40 nm. Also, at each synthesis temperature, different dynamic behavior of the photoluminescence (PL) peak components was observed when ZnS was coated on the surface of the CIS core. These PL peak components are believed to be defect-related emission of CIS/ZnS QDs, and were analyzed by low-temperature PL. Four PL peak components were observed and the change in each PL peak component could be due to cation exchange. The degree of passivation by the ZnS shell at different synthesis temperatures results in a PL quantum yield (QY) of 26–38%. To evaluate the possibility of applying CIS/ZnS QDs to bio-imaging, an experiment to convert the hydrophobic surface of QDs to a hydrophilic one was carried out using a human serum albumin (HSA)/N-hydroxysuccinimide-functionalized six-arm-branched poly(ethylene glycol)(6-arm PEG-NHS) encapsulation method. The 6-armend PEG-NHS was used as an amphiphilic ligand, and its fluorescence intensity was decreased to 57% of that of the initial QDs after fabrication of the QD-HSA/PEG nanocapsules. The size of the nanocapsules was 140 ± 21.6 nm, measured by SEM and TEM.

Introduction

Colloidal semiconductor nanocrystals, including quantum dots (QDs), have drawn attention from the research community because of their unique and efficient optical properties, as well as potential applications such as in bio-imaging, light-emitting-diodes (LEDs),[1,2] and solar cells.[3,4] Typical II–VI QDs, such as CdSe, CdS, and CdTe emit extensive color in the visible range and show a high quantum yield (QY) of ∼80%.[5,6] However, they contain toxic materials (Cd, Te), which limits their application. In response to these considerations, I–III–VI QDs, also termed

Department of Materials Science and Engineering, Korea Advanced Institute of Science and Technology, 291 Daehak-ro, Yuseong-gu, Daejeon 305-338, Republic of Korea. E-mail: dyj@kaist.ac.kr; yoonsung@kaist.ac.kr

† Electronic supplementary information (ESI) available. See DOI: 10.1039/c6ra27045j

‡ These authors contributed equally to this work.

§ Center for Theragnosis, Korea Institute of Science and Technology (KIST), Seoul 136-791, Republic of Korea.

Cd-free QDs, can be suggested as an alternative material. I–III–VI QDs, including CuInS2 (CIS) QDs, have tunable emission in the range of visible to near-infrared (NIR) radiation, large Stokes shifts,[7] and long decay time[8] relative to those of II–VI QDs, and in this light CIS QDs are suitable for application to deep tissue imaging. For bio-applications, especially *in vivo* imaging, not only toxicity but also emission wavelength of QDs is the important concern. In biological systems, there are many visible light absorbers, such as hemoglobin, oxy-hemoglobin, fatty tissue, and water.[9] Visible light emission from QDs can be absorbed by these visible light absorbers, resulting in decreased detectability. Therefore the best candidate emission range of fluorescent probes is 650–900 nm in the NIR range. The emission wavelength of CIS QDs can be tuned by using an off-stoichiometry effect, unlike other QDs which can be tuned by using a size effect. B. K. Chen *et al.* reported that the crystal structure and the optical properties of CIS QDs can be influenced by controlling the [Cu]/[In] molar ratio.[10] Although the emission wavelength of QDs can be tuned in the NIR range, they are restricted in fluorescent applications because of their poor

luminescence efficiency.[11] In order to improve their efficiency, ZnS, having a larger bandgap that is suitable for type 1 band alignment,[12] a crystal structure that is similar the structure of the CIS core, chemical stability, and non-toxicity, was chosen as a shell material.[13] However, cation-exchange, where Zn^{2+} ions readily diffuse into the CIS structure and replace the Cu^+ or In^{3+} ions, occurs during ZnS shell coating. Due to the cation-exchange, the shallow surface of the QDs is alloyed to become $CuInZnS_2$ (CIZS). The size of the core/shell QDs does not decrease but their bandgap does. Consequently, the PL spectra of CIS/ZnS QDs are blue-shifted.[14]

Furthermore, the hydrophilicity has to be considered in order to use QDs in bio-applications. QDs are generally synthesized via organometallic methods, which are hydrophobic, and many researchers encounter difficulties in applying QDs for bio-imaging. One of the proposed methods is an amphiphilic organic/polymer ligand coating (exchange) to transfer QDs into aqueous solution.[15,16] Without detachment of the organic ligand from QDs, the amphiphilic ligand can be attached on the organic ligand by hydrophobic–hydrophobic interaction, and subsequently the outer surface of the QDs is rendered hydrophilic because of the polar parts of the amphiphilic ligand.

In this research, we provide two synthesis methods to obtain NIR-emitting QDs. The first method is to tune the emission wavelength of CIS QDs to the NIR range using an off-stoichiometry effect, controlled by the ratio of two different cation (Cu^+, In^{3+}) reactants. In the second method, in order to retain the NIR-emission wavelength of the emission from the CIS core, we controlled the temperature during ZnS shell coating at various temperatures, 180 °C, 210 °C, 230 °C, and 250 °C. The effect of temperature on inhibiting the cation-exchange phenomenon was explained using a substitutional diffusion mechanism. Additionally, the relation between the blue-shift of the PL spectra and the different dynamic behavior of PL peak components in the blue-shifted PL spectra with varying ZnS shell synthesis temperatures was studied. The resulting QDs were subsequently encapsulated with human serum albumin (HSA)/poly ethylene glycol (PEG) nanocapsules by an oil-in-water (O/W) emulsion method.

Experimental section

Materials

Copper(I) iodide (CuI, 99.995%), indium(III) acetate (In(OAc)₃, 99.99%), 1-dodecanethiol (DDT, 97%), 1-octadecene (ODE, 90%), zinc acetate (Zn(OAc)₂, 99.99%), human serum albumin (HSA, essentially fatty acid free), and dichloromethane (CH₂Cl₂, ≥99.8%) were purchased from Sigma-Aldrich, and N-hydroxysuccinimide-functionalized six-arm-branched poly(ethylene glycol)(6-arm PEG-NHS, MW = 15 kDa) was purchased from Sun-bio.

Synthesis of CuInS₂ core

The basic synthetic procedure is available in a previously published article.[13] 0.4 mmol of CuI, 0.2 mmol of In(OAc)₃, and 4 ml of DDT (16.6 mmol) were mixed with 16 ml of ODE in a 50 ml three-neck flask. The reaction mixture was degassed under a vacuum at 60 °C and stirred for 30 min. The solution was subsequently heated to 210 °C and kept for 90 min under a N₂ atmosphere. The color of the CIS core solution was changed from transparent yellow to turbid dark brown. [Cu]/[In] ratios were changed from 0.25 to 2. Afterward, the solution was cooled to 60 °C and the remaining Cu precursor was removed by precipitation without an additional polar solvent (6000 rpm, 4 min).

Synthesis of CuInS₂/ZnS core/shell QDs

5 ml of as-prepared CIS core and 0.5 mmol of Zn(OAc)₂ were mixed in a 50 ml three-neck flask and degassed under a vacuum at 60 °C with stirring for 30 min. The solution was then heated to growth temperature and the temperature was kept for proper duration at 180 °C, 210 °C, 230 °C, and 250 °C, respectively. Aliquots were extracted at each synthesis time as time passed, and transferred to quartz cuvettes to record the emission wavelength of each sample. After synthesis, the solution was cooled to room temperature and purified by precipitation with an excess amount of ethanol. The precipitant was re-dispersed in chloroform for characterization.

Fabrication of QD-HSA/PEG nanocapsule for bio-imaging

Its basic synthetic procedure is available in a previously published article.[15] 5 mg of CIS/ZnS QDs and 5.65 mg of 6-armed N-hydroxysuccinimide (NHS)-functionalized polyethylene glycol (PEG) were dissolved in 0.5 ml of dichloromethane (DCM). HSA solution was prepared by dissolving 2.5 mg of HSA in 10 ml of deionized (DI) water. The mixture of QDs and NHS-PEG was dropped into the HSA solution (pH 9) saturated with dichloromethane and subsequently sonicated at low temperature (<4 °C) for 5 min using a Branson Sonifier 450 (frequency of 20 kHz with a duty cycle of 20 and an output control of 3.5). The emulsified solution was transferred to a rotary evaporator and the dichloromethane was rapidly evaporated under a reduced pressure at 45 °C. After evaporation, the dried QD-HSA/PEG nanocapsule was dispersed in 3 ml of DI water for further characterization.

Characterization

Photoluminescence (PL) spectra were recorded using a Hitachi F-7000 luminescence spectrometer and absorption spectra were obtained on a Shimadzu UV-1800 spectrophotometer. The QY were measured by comparing an integrated emission of QDs in chloroform with emission of Rhodamine 6G in ethanol. (QY of R6G = 95%). Transmission electron microscopy (TEM) images were taken using a JEM-ARM200F. Powder X-ray diffraction (XRD) patterns were obtained using a D/MAX-RB (12 kW) from RIGAKU. Low-temperature PL spectrum was taken using a Lab-RAM HR UV/Vis/NIR PL and SEM images were taken by a Hitachi S-4800. Zeta potential of QD-HSA/PEG nanocapsule was measured using the particle size analyzer (Malvern, Zeta sizer nano zs). The X-ray photoelectron spectroscopy (XPS) analysis was conducted using multi-purpose X-ray photoelectron

spectroscopy (Sigma probe, Thermo VG scientific). The samples for XPS analysis were prepared by spin-casting QD solution on a glass substrate. The measured XPS spectra were calibrated with the position of C 1s peak at 284.6 eV.

Results and discussion

Structural and optical characterization of CIS core

The structural analysis of the CIS core was carried out by TEM and XRD. The TEM image presented in Fig. 1a shows that a tetrahedron-shaped CIS core was synthesized (size: 4–5 nm). The tetragonal structure of CIS showed three main peaks, corresponding to (112), (220)/(204) and (312)/(116) planes, as referenced in JCPDS (Fig. 1b). In the case of [Cu] : [In] = 1 : 1, all three peaks were well matched to those of bulk tetragonal CIS. However, as the portion of Cu increased, all three peaks were shifted to smaller angles, on the other hand, the peaks of the sample with [Cu] : [In] = 0.25 : 1 were slightly shifted to larger angles. These shifts of the XRD patterns indicate that crystal distortions occurred due to the off-stoichiometry effect. Crystal distortions could be generated, due to the change in bonding of either Cu^+ or In^{3+} to the same cation sites in the chalcopyrite structure, and the difference in the bonding length between Cu–S and In–S, and these might cause the shift toward lower angle. The (PL) spectra with different [Cu] : [In] ratios are shown in Fig. 2. As the portion of Cu was increased, the PL peaks were red-shifted from 680 nm to 850 nm. In the case of the Cu-rich CIS core, repulsion between the d-orbital of Cu and the p-orbital of S is enhanced due to the large amount of Cu^+ ions in the CIS structure, and subsequently the valence band of the CIS QDs increases and its intra-band gap also changes.[17] PL QY of the CIS core synthesized with [Cu] : [In] = 0.25 : 1 was around 1%. More crystal distortions ([Cu] : [In] = 1 : 1 to [Cu] : [In] = 2 : 1) increase the defect concentration and QY (up to 4%); however, an excessive amount of distortions leads to a decrease of QY due to quenching of exciton carriers.[18] When the ratio of [Cu]/[In] was over 2, no PL emission was observed and a CIS core could not be synthesized. Additionally, each broad emission peak indicates the emission processes of the CIS core are related to surface or intrinsic donor–accepter defect levels.[19]
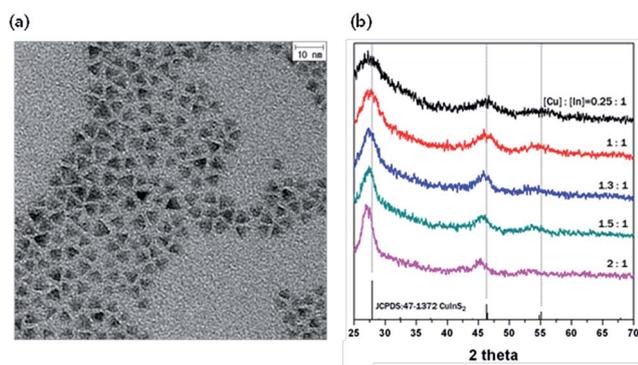

Fig. 1 (a) TEM image of CIS core when [Cu] : [In] = 2 : 1, size = 4–5 nm and tetrahedral structure of CIS core. (b) XRD patterns of CIS core as a function of [Cu] : [In] ratios, 36–1450.
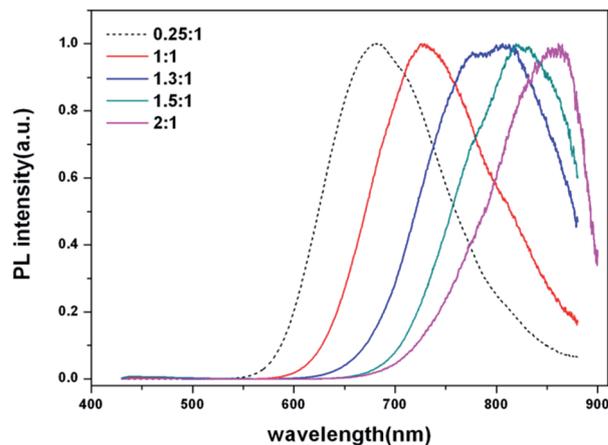

Fig. 2 PL spectra of CIS core with different [Cu] : [In] ratios. The emission wavelength of maximum peak is 681 nm, 726 nm, 806 nm, 820 nm, and 850 nm, respectively (left to right).

Structural and optical characterization of CIS/ZnS core/shell QDs

The CIS core in which the [Cu] : [In] ratio is 2 : 1 and the emission wavelength is 850 nm was chosen to prepare the CIS/ZnS core/shell QDs. The ZnS shell was grown by adding Zn acetate as a Zn precursor without an additional S precursor to the CIS core solution under a N_2 atmosphere at 60 °C and maintained at various temperatures: 180 °C, 210 °C, 230 °C, and 250 °C.

Fig. 3a shows XRD patterns corresponding to four different CIS/ZnS QDs. After the samples were coated by a ZnS shell, three main peaks were shifted to larger angles, which match with XRD peaks of ZnS. These shifts mean indicate that formation of the ZnS shell occurs by over-coating or CIZS alloying by inter-diffusion. According to TEM images shown in Fig. 3b–f, the size of the core/shell QDs does not decrease but their bandgap increases due to the cation-exchange. A CIZS alloy could be generated based on unchanged size of the CIS/ZnS core/shell particle compared to that of the CIS core. As the synthesis temperature increased, a shift to larger diffraction angle from ZnS was observed. This indicates that a larger amount of Zn^{2+} diffused into the CIS structure and alloyed to become CIZS, which contains more Zn^{2+} ions. Based on the XRD data, we could also confirm structural rigidity of CIS/ZnS QDs. As the temperature increased, the pattern became sharper with better signal-to-noise ratios, and these results showed that the crystallinity was improved due to diffusion of Zn^{2+} ions into the CIS core with occupation of vacancies and other defects.

We conducted an elemental analysis (XPS) on the CIS core synthesized at 210 °C and CIS/ZnS core/shell QDs grown at 210 °C by utilizing X-ray photoelectron spectroscopy. The XPS spectra and the elemental analysis data for Cu, In, S, Zn are shown in Fig. S1 and Table S1,† respectively. For both CIS core and CIS/ZnS core/shell QDs, some distinctive peaks appeared in common at ~952 eV and ~932 eV corresponding to Cu 2p 1/2 and Cu 2p 3/2, respectively, and at ~452 eV, ~444 eV associated with In 3d 3/2 and In 3d 5/2, respectively, and at ~162 eV
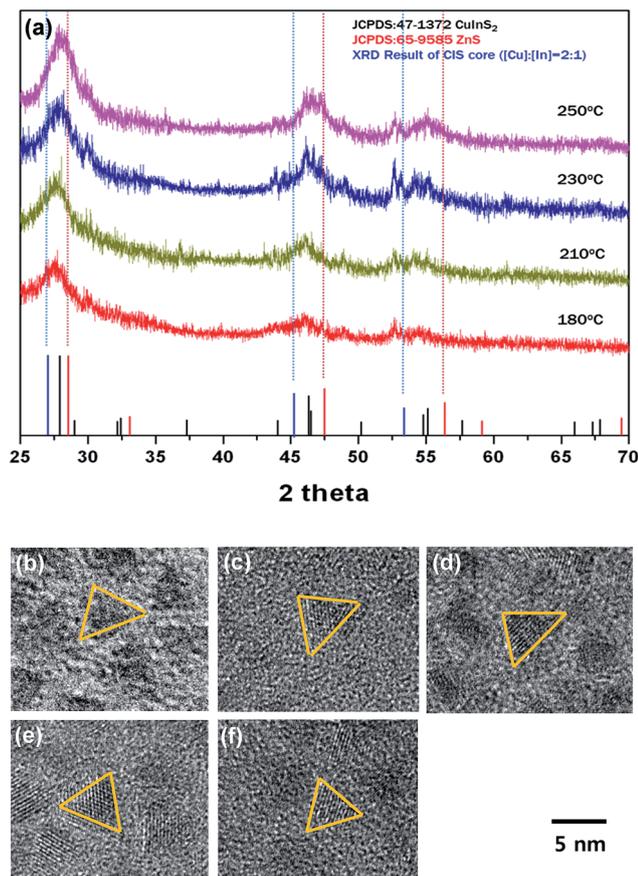
Fig. 3 (a) XRD patterns corresponding to four different CIS/ZnS QDs synthesized at different temperatures, 180 °C, 210 °C, 230 °C, and 250 °C, respectively (bottom to top). TEM images of (b) CIS core ([Cu] : [In] = 2 : 1) and CIS/ZnS QDs synthesized at (c) 180 °C, (d) 210 °C, (e) 230 °C, and (f) 250 °C, respectively. All samples have a tetrahedron structure and the size is (b) 4.0–5.0 nm (c) 180 °C: 4.6–5.4 nm (d) 210 °C: 4.2–5.4 nm (e) 230 °C: 4.5–5.5 nm (f) 250 °C: 4.0–5.5 nm.

corresponding to S 2p 1/2. Two peaks which are exhibited in Zn 2p region and located at ∼1044 eV and ∼1021 eV were shown for CIS/ZnS core/shell QDs, while any signal indicating the presence of Zn was not shown in the XPS spectra for CIS core. The contribution of the signals for each atomic constituent was shown in Table S1.† For CIS core, the compositional ratios of Cu, In, and S were 26.7, 21.9, and 51.4, respectively. After ZnS shell formation, the ratio of S was 78.2, which indicates S-rich surface stoichiometry of the ZnS shell.

Absorption spectra of CIS/ZnS QDs with different shell coating temperatures are shown in Fig. S2.† At lower temperature, for example, 180 °C and 210 °C, the absorption spectra were unchanged, but at higher temperature, 230 °C and 250 °C, the absorption spectra were blue-shifted as the duration of synthesis increases. Comparing the absorption spectra of all samples that were synthesized for the same duration, the absorption spectra were more blue-shifted with increasing synthesis temperature (Fig. S3†). The blue-shift of the absorption spectra reflects a reduction of core size by cation-exchange. Therefore, the smaller blue-shift in the absorption spectra

recorded at lower temperature indicates less reduction of core size.

After finishing ZnS shell coating for all samples, the PL intensity increased due to the stronger quantum confinement effect by shell passivation (Fig. 4). The temporal evolution of the emission spectra of CIS/ZnS QDs during ZnS shell coating at 230 °C and 250 °C, respectively, is shown in Fig. 4a and b. A blue-shift of PL was already detected at the beginning stages, and the PL spectra were blue-shifted proportionally as the synthesis time increased. However, at the terminal stage, the PL peaks were degraded. On the other hand, for the samples prepared at 180 °C and 210 °C, there was no degradation of PL peaks, with PL increased straightly (Fig. 4c and d). In order to access the amount of blue-shift as a function of synthesis time at lower synthesis temperature, we synthesized CIS/ZnS QDs at 180 °C and 210 °C for long duration of about 570 min and 660 min until the PL spectra degraded, respectively (Fig. S4†). In the case of the sample prepared at 180 °C, the PL spectra maintained the initial emission wavelength for longer duration than in the case of the sample prepared at 210 °C (210 °C: 90 min, 180 °C: 300 min). Therefore, the blue-shift of the PL spectra was inhibited effectively compared to the samples synthesized at higher temperatures.

The tendencies of blue-shift of absorption and PL spectra can be explained by the effective size of the CIS core becoming smaller due to the cation-exchange phenomenon. During ZnS shell coating, the Zn^{2+} ions diffused into the surface of the CIS core, and replaced both Cu^+ and In^{3+} ions and made a CIZS alloy. The effective size of the CIS core consequently became smaller. The present results show that the emission wavelengths of CIS/ZnS QDs tend to maintain their peak position and their intensities increase as the shell coating temperature decreases, and this small blue-shift of the PL spectra at low temperature also indicates that cation exchange was suppressed at low temperature.

The classic substitutional diffusion theory suggests that the activation energy for diffusion is determined by temperature, and the governing equations are given in eqn (1)–(3), where A
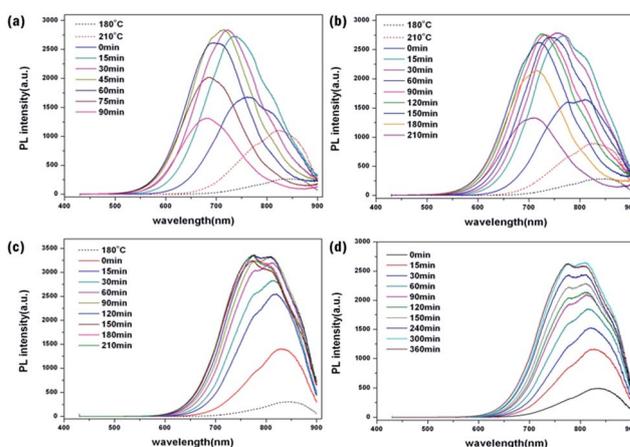

Fig. 4 Temporal evolution of emission spectra of CIS/ZnS QDs during ZnS shell coating at (a) 250 °C, (b) 230 °C, (c) 210 °C, and (d) 180 °C, respectively.

and B are two different atoms to substitutionally diffuse, Q is the activation enthalpy for diffusion, and C is the concentration of atoms, respectively.[20]

$$J = D_{A,B} \frac{\delta C_{A,B}}{\delta x} \qquad (1)$$

$$D_{A,B} = D_{A0,B0} \exp\left(-\frac{Q_{A,B}}{RT}\right) \qquad (2)$$

$$J_V = (D_A - D_B)\frac{\partial C_A}{\partial x} \qquad (3)$$

These equations are Fick's first law, diffusion coefficient, and total flux, respectively. The fraction of atoms with more than the mean energy, which is expressed by $\left(\exp\left(-\frac{Q_{A,B}}{RT}\right)\right)$, is needed to exchange different cations. The diffusion coefficient decreases exponentially with decreasing temperature. Therefore, the diffusion rate becomes lower at lower temperature compared to the rate at higher temperature. Consequently, a small amount of Zn^{2+} ions diffuse into the surface of the CIS core at lower temperature due to weak driving force for diffusion (Fig. 5). The cation-exchange phenomenon occurring during ZnS coating follows this classic substitutional diffusion theory and can be inhibited by decreasing the synthesis temperature. Therefore, at the lower synthesis temperatures for the ZnS shell, NIR-emitting QDs could be synthesized more effectively. However, the blue-shift of the PL spectra is not simply explained by the PL peak movement, but it includes the dynamic behavior of the PL peak components. The normalized PL spectra of CIS/ZnS QDs shows that one PL spectrum may contain several peak components rather than a single component, and each component shows different dynamic behavior as the duration of synthesis increases (Fig. 6). In the PL spectra, multiple emissions were observed for CIS/ZnS QDs. The different evolution trends of the PL peak components are summarized in Table 1 with synthesis temperature and duration. The components of the PL spectrum from the CIS core were analysed by low-temperature PL (Fig. 6e). According to the low-temperature PL spectrum, that from the CIS core is composed of four peak components; 685 nm, 750 nm, 800 nm and 865 nm, with intervals of about 50 nm. These four PL peaks indicate that at least four different defect levels affect the emission process, in contrast with other kinds of QDs that emit
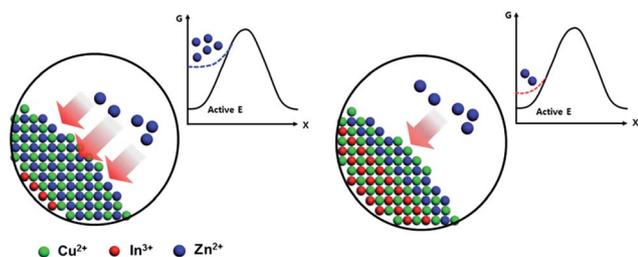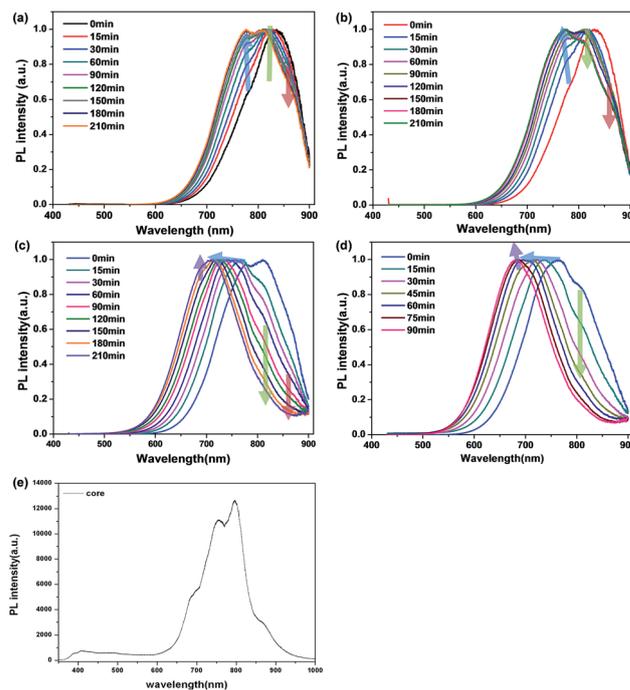

Fig. 6 Normalized PL spectra of CIS/ZnS QDs with (a) 180 °C, (b) 210 °C, (c) 230 °C and (d) 250 °C, respectively. Each spectrum contains three or four peak components and different evolution of peak components was observed. Arrows indicate different evolution trends of each PL peak component (e) low-temperature PL spectrum of CIS core measured at 4 K. (a) Relatively high T and (b) low T.

through band-edge emission. These emission wavelengths of peak components are also well matched with those of peak components of the samples for 180 °C, 210 °C, 230 °C, and 250 °C, respectively.

The four peak components shown in Fig. 6e are originating from the various defect constituents present on the Cu-rich CIS-based QDs as shown in the Fig. S5.† The peak of 865 nm corresponds to the transition between In_{cu} and V_{in}, and the peaks of 800 nm and 750 nm are associated with the recombination between In_i and V_{in} and V_s and V_{in}, respectively. The highest energy (680 nm) is come from the transition between V_s to valence band of QDs.[21,22]

The low-temperature PL data reveal that the PL peak components in PL results can be reasonable. According to the present results, temperature control also can influence the evolution of the PL peak components in the PL spectra. As the synthesis temperature increased, the higher energy peaks became dominant but the lower energy peaks became minor in the blue-shifted PL spectra of CIS/ZnS. The peak components are related to the emission process through defect levels of CIS/ZnS QDs. The change in peak components also indicates a change in the emission process between different defect levels. In terms of the energy band diagram, the concentration of defect levels related to lower energy peaks could be decreased due to cation exchange during the ZnS shell coating while the concentration of defect levels related to higher energy peaks could be increased. Therefore, we could assume that the cation-exchange between Zn^{2+} ions and In^{3+} ions can affect each

Fig. 5 Temperature dependence of inter-diffusion of Zn ions on the surface of core. (a) Relatively high T and (b) low T.

Table 1 The observation of the different evolution trends of three or four PL peak components during ZnS coating with different temperature

Temperature	PL	Peak 1 (nm)	Peak 2 (nm)	Peak 3 (nm)	Peak 4 (nm)
180 °C	Wavelength	—	775 nm	815 nm	865 nm
	Proportion of PL intensity	—	Increase	Maintain	Decrease
	Position	—	Blue-shift	Maintain	Maintain
210 °C	Wavelength		775 nm	815 nm	865 nm
	Proportion of PL intensity		Increase	Decrease	Decrease
	Position		Blue-shift	Maintain	Maintain
230 °C	Wavelength	690 nm	720–770 nm	810 nm	865 nm
	Proportion of PL intensity	Increase	Maintain	Decrease	Decrease
	Position	Maintain	Blue-shift	Maintain	Maintain
250 °C	Wavelength	680 nm	710–760 nm	810 nm	—
	Proportion of PL intensity	Increase	Maintain	Decrease	—
	Position	Maintain	Blue-shift	Maintain	—

concentration of In_i and In_{Cu} defect levels, but further analysis of this is required.

The study on the PL decay of QDs was investigated by utilizing time-correlated single photon counting (TCSPC) technique, and the PL decay curves of CIS and CIS/ZnS QDs were characterized at 685 nm, and 800 nm (Fig. S6†). The PL decay curves were de-convoluted into three exponential components (τ_1, τ_2, and τ_3). For CIS-based QDs, fast decay component (τ_1) is associated with the emission from the surface/interface-trapped states, and the slow ones (τ_2 and τ_3) correspond to the defect-related donor–acceptor transitions.[23] The average PL lifetimes increased from 150.6 ns to 296.0 ns for CIS core, and from 317.3 ns to 513.9 ns for CIS/ZnS core/shell QDs, as the PL spectral region moves at longer wavelengths (from 685 nm to 800 nm). After ZnS shell formation, the average PL lifetime increased, and the decay amplitude fraction of the fast decay component (τ_1) decreased for both wavelengths (24.94% to 14.29% at 685 nm, and 23.41% to 9.18% at 800 nm), which indicates the increased rate of the defect-related donor–acceptor transition as the surfaces-state varies.[23]

The enhancement of QY as a function of synthesis duration is shown in Fig. S7.† In the initial stages of ZnS shell coating, QY increased and later saturated at about 30%. The improvement of QY is determined by diffusion of Zn^{2+} ions on the shallow surface of the CIS core. Therefore, if a proper amount of Zn^{2+} ions diffuse and occupy the non-radiative sites of shallow surface of CIS core, the QY will be strongly enhanced during ZnS shell coating without regard to the synthesis temperature. However, as the temperature became higher, the rate of increase of QY, which means the rate of reaching the maximum value of QY, increased relative to that at low temperature. As more Zn^{2+} ions diffuse into the core, the cation-exchange occurs more actively at high temperature, the Zn^{2+} ions rapidly occupy the trap sites on the surface of the core, and finally the rate of increase of the QY becomes faster.

In addition, a decreasing QY was observed in the end stages of shell growth, and the QY decreased faster at high temperature than at low temperature (250 °C: after 75 min, 230 °C: 150 min, 210 °C: 210 min, 180 °C: not decreasing until 660 min). Similar to the explanation of the increasing rate of QY, at high temperature, the Zn monomer consumption rate becomes faster because of active cation-exchange, and in the end stages, the degradation of QDs can occur because of an insufficient ZnS source with continuous heating. In this study, the maximum value of QY was 38% at 720 nm and the average QY was 30% from 720 nm to 810 nm. Compared to the recently published values of QY for NIR-emitting CIS/ZnS QDs, highly efficient NIR emitting CIS/ZnS QDs were synthesized.[13,24–26]

Characterization of CIS/ZnS QDs-HSA/PEG nanocapsules

For potential applications of QDs to bio-imaging, the synthesized CIS/ZnS QDs were encapsulated within shell-crosslinked nanocapsules (NCs) using HSA and 6-armed PEG, which can generate a very stable, biocompatible interface suitable for long-term blood circulation. NCs were fabricated by using CIS/ZnS QDs synthesized at 210 °C for 60 min, having a QY of 29%. CIS/ZnS QDs and 6-armed PEG–N-hydroxysuccinimide (NHS) were dissolved in dichloromethane, injected into aqueous HSA solution (1 mg ml⁻¹), and sonicated to prepare an O/W emulsion. During this process, the NHS terminal groups of the PEG molecule were conjugated to the primary amines of HSA at the surface and formed cross-linked shell layers comprising PEG and HSA.[27] Fig. 7a shows the dispersibility of the QD-HSA/PEG nanocapsule in DI water compared to initial QDs in dichloromethane. Both samples were transparent, and thus not only the initial QDs but also the QD-HSA/PEG nanocapsules were well dispersed in each solution. Also, under 365 nm UV excitation, the QD-HSA/PEG nanocapsule solution exhibited the same emission color as the initial hydrophobic QDs, as shown in the optical micrograph (Fig. 7b). The emission wavelength was almost retained after fabrication of nanocapsules but the fluorescent intensity decreased to 57% of that of the initial QDs (Fig. 7c). The dispersibility in DI-water and maintenance of the optical property of QDs indicate that the initial hydrophobic QDs were changed to hydrophilic QDs. The structural properties of the QD-HSA/PEG nanocapsules are shown by SEM and TEM images. In Fig. 8a, the SEM images show the shape and size distribution of the nanocapsules. Spherical-shaped nanocapsules were observed without any significant aggregation. The size of the nanocapsules is about 140 ± 21.6 nm with a narrow distribution. TEM images also show the shape of the nanocapsules, including inorganic quantum dots and organic
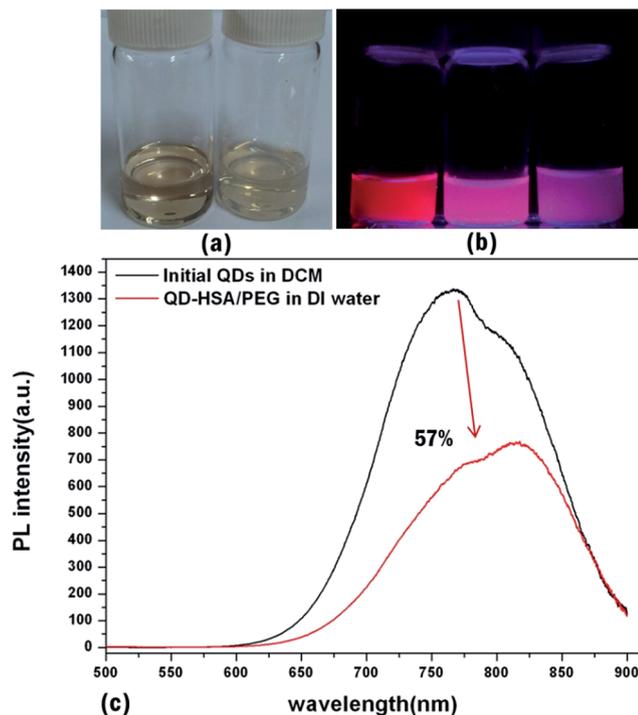
Fig. 7 (a) Photoimages of CIS/ZnS QDs in DCM (left) and QD-HSA/PEG nanocapsule in DI water (right) and (b) under 365 nm UV-lamp, (left) initial QDs (middle) QD-HSA/PEG nanocapsule after filtering (right) QD-HSA/PEG nanocapsule before filtering. (c) PL spectrum of initial QDs and QD-HSA/PEG nanocapsule. PL intensity of nano-capsule: 57% of initial QDs. (a) Relatively high T and (b) low T.
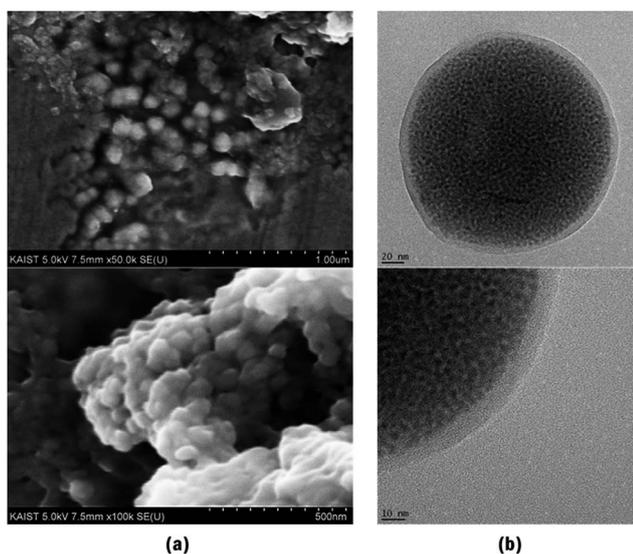

Fig. 8 (a) SEM images, (b) TEM images of QD-HSA/PEG nanocapsules.

HSA/PEG shell (Fig. 8b). The zeta potential of the prepared QD-loaded HSA/PEG nanocapsules was −16.7 mV, which indicates the presence of negatively charged HSA (the isoelectric point of HSA is about 5) on the surface of the NCs. Inorganic CIS/ZnS QDs have 4–5 nm tetrahedron structures inside the shell, and organic shell is observed as a shaded region surrounding QDs

because the organic shell does not have crystallinity (thickness: 9 nm). Therefore, from SEM and TEM images, it is found that QD-HSA/PEG nanocapsules with appropriate hydrodynamic diameter were fabricated without agglomeration.

Conclusions

We have described the synthesis process of efficient NIR-emitting CIS/ZnS QDs by controlling the ZnS shell synthesis temperature. The CIS core was prepared using an off-stoichiometry effect, and the proper [Cu] : [In] ratio was 2 : 1 and the tuned emission wavelength was 850 nm (size: 4–5 nm). However, during ZnS shell coating to improve the QY, an adverse effect was observed because of cation-exchange. To inhibit cation-exchange, we controlled the temperature during ZnS shell synthesis, at 180 °C, 210 °C, 230 °C, and 250 °C, respectively. At the lowest temperature, 180 °C, the least Zn^{2+} ions diffused into the CIS core and the diffusion rate became slower than that at higher temperature because the activation energy to diffuse was affected by temperature. Temperature control during synthesis of the ZnS shell led to not only a blue-shift but also evolution of the PL peak components in the PL spectra of CIS/ZnS QDs. The difference in the dynamic behavior of PL peak components during ZnS shell synthesis at the different synthesis temperatures indicates that the degree of Zn^2 ion diffusion during ZnS shell coating could affect the emission process through defect levels of CIS/ZnS QDs. Consequently, CIS/ZnS QDs, having 810 nm emission wavelength and 30% of QY, were synthesized at 180 °C with inhibition of both cation-exchange and blue-shift of PL spectra. Finally, in order to apply the synthesized NIR-emitting CIS/ZnS QDs to bio-imaging, QDs were encapsulated as a form of QD-HSA/PEG nanocapsules by the O/W emulsion method and successfully transferred to an aqueous phase. As shown by these results, because the nanocapsules were fabricated to appropriate size for bio-imaging (140 nm ± 21.6 nm), and finally the NIR-emitting CIS/ZnS QDs synthesized with inhibited cation-exchange have the potential application to *in vivo* imaging.

Acknowledgements

References

1 J. M. Caruge, J. E. Halpert, V. Wood, V. Bulovic and M. G. Bawendi, *Nat. Photonics*, 2008, **2**, 247.
2 J. L. Zhao, J. A. Bardecker, A. M. Munro, M. S. Liu, Y. H. Niu, I. K. Ding, J. D. Luo, B. Q. Chen, A. K. Y. Jen and D. S. Ginger, *Nano Lett.*, 2006, **6**, 463.
3 J. M. Lee, B. H. Kwon, H. I. Park, H. Kim, M. G. Kim, J. S. Park, E. S. Kim, S. Yoo, D. Y. Jeon and S. O. Kim, *Adv. Mater.*, 2013, **25**, 2011.

4 I. Robel, V. Subramanian, M. Kuno and P. V. Kamat, *J. Am. Chem. Soc.*, 2006, **128**, 2385.

5 C. D. Donega, S. G. Hickey, S. F. Wuister, D. Vanmaekelbergh and A. Meijerink, *J. Phys. Chem. B*, 2003, **107**, 489.

6 D. V. Talapin, A. L. Rogach, A. Kornowski, M. Haase and H. Weller, *Nano Lett.*, 2001, **1**, 207.

7 S. L. Castro, S. G. Bailey, R. P. Raffaelle, K. K. Banger and A. F. Hepp, *J. Phys. Chem. B*, 2004, **108**, 12429.

8 Y. Hamanaka, T. Kuzuya, T. Sofue, T. Kino, K. Ito and K. Sumiyama, *Chem. Phys. Lett.*, 2008, **466**, 176.

9 X. X. He, J. H. Gao, S. S. Gambhir and Z. Cheng, *Nanomaterials*, 2012, **2**, 92.

10 B. K. Chen, H. Z. Zhong, W. Q. Zhang, Z. A. Tan, Y. F. Li, C. R. Yu, T. Y. Zhai, Y. S. Bando, S. Y. Yang and B. S Zou, *Adv. Funct. Mater.*, 2012, **22**, 2081.

11 R. G. Xie, M. Rutherford and X. G. Peng, *J. Am. Chem. Soc.*, 2009, **131**, 5691.

12 P. Reiss, M. Protiere and L. Li, *Small*, 2009, **5**, 154.

13 L. Li, T. J. Daou, I. Texier, T. K. C. Tran, Q. L. Nguyen and P. Reiss, *Chem. Mater.*, 2009, **21**, 2422.

14 J. Park and S. W. Kim, *J. Mater. Chem.*, 2010, **21**, 3745.

15 J. Y. Lee, K. H. Bae, J. S. Kim, Y. S. Nam and T. G. Park, *Biomaterials*, 2011, **32**, 8635.

16 M. Michalska, A. Florczak, H. Dams-Kozlowska, J. Gapinski, S. Jurga and R. Schneider, *Acta Biomater.*, 2016, **35**, 293–304.

17 W. S. Song and H. Yang, *Chem. Mater.*, 2012, **24**, 1961.

18 H. Z. Zhong, Z. L. Bai and B. S. Zou, *J. Phys. Chem. Lett.*, 2012, **3**, 3167.

19 H. Zhong, Y. Zhou, M. Ye, Y. He, J. Ye, C. He, C. Yang and Y. Li, *Chem. Mater.*, 2008, **20**, 6434.

20 D. A. Porter and K. E. Easterling, *Phase transformation in metals and alloys*, CRC Press, USA, 2003.

21 J. J. M. Binsma, L. J. Giling and J. Bloem, *J. Lumin.*, 1982, **27**, 35.

22 H. Y. Ueng and H. L. Hwang, *J. Phys. Chem. Solids*, 1989, **50**, 1297.

23 J. Seo, S. Raut, M. Abdel-Fattah, Q. Rice, B. Tabibi, R. Rich, R. Fudala, I. Gryczynski, Z. Gryczynski, W.-J. Kim, S. Jung and R. Hyun, *J. Appl. Phys.*, 2013, **114**, 094310.

24 W. D. Xiang, H. L. Yang, X. J. Liang, J. S. Zhong, J. Wang, L. Luo and C. P. Xie, *J. Mater. Chem. C*, 2013, **1**, 2014.

25 D. W. Deng, Y. Q. Chen, J. Cao, J. M. Tian, Z. Y. Qian, S. Achilefu and Y. Q. Gu, *Chem. Mater.*, 2012, **24**, 3029.

26 K. Yu, P. Ng, J. Y. Ouyang, M. B. Zaman, A. Abulrob, T. N. Baral, D. Fatehi, Z. J. Jakubek, D. Kingston, X. H. Wu, X. Y. Liu, C. Hebert, D. M. Leek and D. M. Whitfield, *ACS Appl. Mater. Interfaces*, 2013, **5**, 2870.

27 R.-S. Liu, *Phosphors, Up Conversion Nano Particles, Quantum Dots and Their Applications*, Springer, Singapore, 2016, vol. 2, pp. 464–465.